ACS Catalysis

Letter

pubs.acs.org/acscatalysis

Interface Engineering in Nanostructured Nickel Phosphide Catalyst for Efficient and Stable Water Oxidation

Junyuan Xu,[†] Xian-Kui Wei,[‡] José Diogo Costa,[†] José Luis Lado,[§] Bryan Owens-Baird,[∥] Liliana P. L. Gonçalves,[†] Soraia P. S. Fernandes,[†] Marc Heggen,[‡] Dmitri Y. Petrovykh,[†] Rafal E. Dunin-Borkowski,[‡] Kirill Kovnir,[∥] and Yury V. Kolen'ko*[,†]

[†]International Iberian Nanotechnology Laboratory, Braga 4715-330, Portugal

[‡]Ernst Ruska-Centre for Microscopy and Spectroscopy with Electrons and Peter Grünberg Institute, Forschungszentrum Jülich GmbH, 52425 Jülich, Germany

[§]QuantaLab, International Iberian Nanotechnology Laboratory, Braga 4715-330, Portugal

[∥]Department of Chemistry, University of California, Davis, Davis, California 95616, United States

Supporting Information

ABSTRACT: An approach to significantly enhance the performance of the cost-effective nickel phosphide catalyst for electrochemical water oxidation has been developed via interfacing with Mg oxide-hydroxide. We have synthesized Ni_2P nanoparticles anchored on $Mg_2O(OH)_2$-like phase supported on carbon paper. During the oxygen evolution reaction, the well-defined Ni_2P nanoparticles serve as precursors for the immediate formation of active and stable nanostructured nickel hydroxide catalyst. As the anode for the oxygen evolution reaction in an alkaline electrolyte, the electrode shows a modest Tafel slope of 48 mV dec^{-1} and a large turnover frequency of 0.05 s^{-1} at an overpotential of 0.4 V. Microstructure and composition studies of the catalyst suggest that interfacial strain between Mg- and Ni-containing phases is responsible for high catalytic activity. A significant increase in catalytic activity upon the combination of magnesium compound and transition-metal phosphide suggests an interesting strategy for the controlled and reproducible preparation of active Earth-abundant oxygen-evolving catalysts.

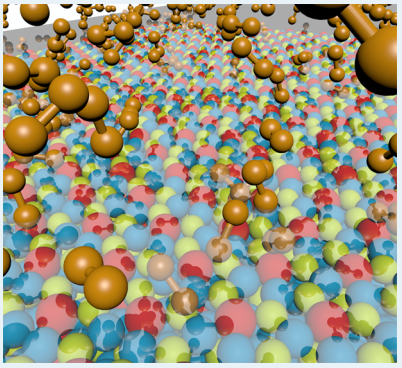

KEYWORDS: *OER, Ni_2P, nanoparticles, core−shell, strain, electrocatalysis*

Hydrogen serves as a fundamentally important renewable energy vector for emerging zero-emission fuel cell technology.[1] In the context of sustainable H_2 production, water electrolysis (WE) provides an attractive and direct route to generate H_2, fulfilling both efficiency and gas purity requirements.[2] Unfortunately, the widespread implementation of WE remains challenging because of the slow kinetics of the oxygen evolution reaction (OER) taking place at the anode.[3] In terms of activity and durability, the best catalysts for the OER are Pt-group metals (PGMs), including RuO_2 and IrO_2.[4] However, PGMs are critical and expensive elements, which limit the expansion of WE technology to large-scale deployment. Recent advances in the search of new Earth-abundant catalysts have indicated that water oxidation can be mediated by transition-metal-containing compounds, such as perovskites, oxides, hydroxides, and oxo-hydroxides,[5] thereby providing feasible alternatives to PGM-based catalysts. Despite significant progress in this area, however, the number of PGM-free materials that can efficiently catalyze water oxidation for extended periods of time is still limited.[6]

In our recent work,[7] we found that a mixed Fe−Ni phosphide ($Fe_{0.2}Ni_{0.8}P_2$) supported on carbon paper (CP) catalyzes the OER in alkaline media, showing reasonably high activity. More importantly, we demonstrated[7] that metal phosphides serve as precursors for the *in situ* generation of the active catalyst during water oxidation. The catalyst can be designed by reliable and simple computational methods on the basis of *d*-band theory.[8] In our earlier work,[9] we predicted and then experimentally realized highly active and stable catalysts for water reduction by utilizing chemical doping of Ni phosphides with the *p*-metal Al. The enhanced catalytic performance was driven by a broadening of the Ni 3d-orbital contribution and an increase in covalent bonding character.

Encouraged by the potential of the chemical doping approach, we decided to explore the possibility of developing an active catalyst for water oxidation by combining Ni_2P with the alkaline-earth s-metal Mg. Instead of forming the ternary Mg−Ni phosphide catalyst, we obtained Ni_2P nanoparticles anchored on a $Mg_2O(OH)_2$-like phase supported on CP. The produced catalyst for water oxidation is highly active and stable. The catalyst is supported on CP and has a low mass density of ~1.3 mg cm^{-2}, thereby fulfilling the requirements for a cost-

Received: June 15, 2017
Revised: July 11, 2017
Published: July 13, 2017

DOI: 10.1021/acscatal.7b01954
ACS Catal. 2017, 7, 5450−5455

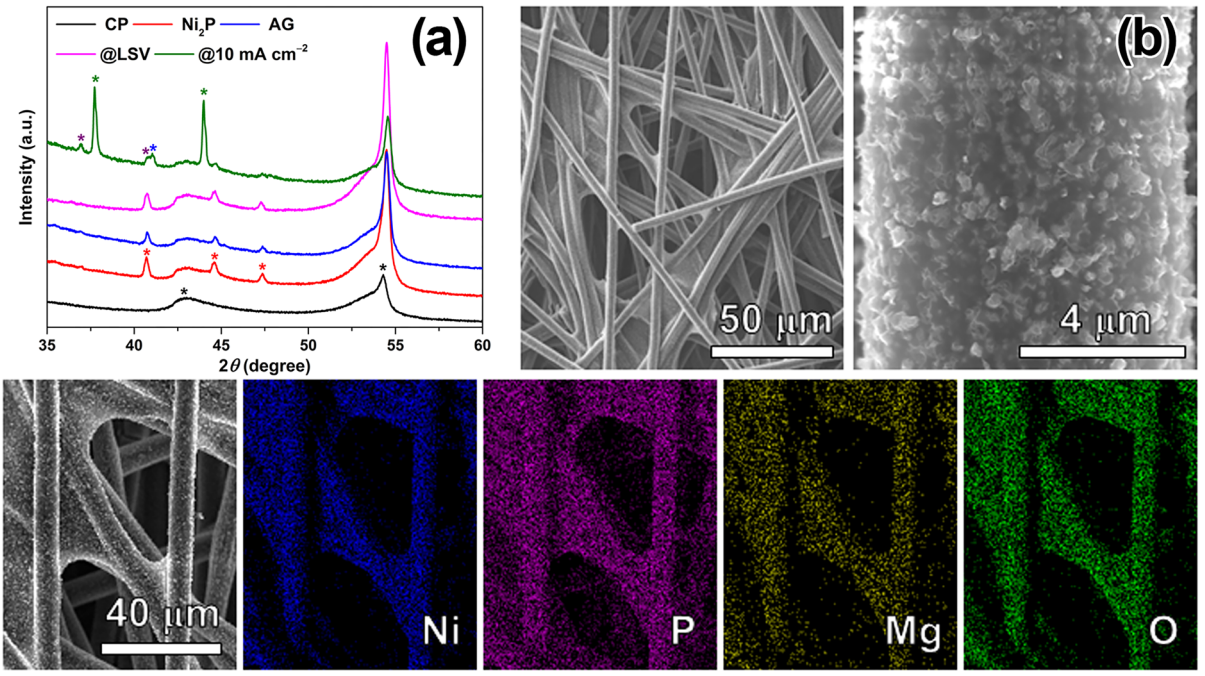

Figure 1. (a) XRD patterns of CP, control Ni_2P, and as-grown Mg-modified Ni_2P (AG), linear sweep voltammetry (LSV)-tested Mg-modified Ni_2P, and durability-tested Mg-modified Ni_2P sample. Black, red, green, purple, and blue asterisks correspond to the positions of the most intense Bragg reflections expected for hexagonal C (ICDD No. 00-041-1487), hexagonal Ni_2P (ICDD No. 04-008-0034), cubic NiO (ICDD No. 04-007-8202), monoclinic β-NiO(OH) (ICDD No. 00-059-0464), and hexagonal $Mg_2O(OH)_2$ (ICDD No. 04-014-8450), respectively. (b) SEM images of the as-grown Mg-modified Ni_2P on CP, acquired at different magnifications, together with EDX mapping of Ni, P, Mg, and O.

effective electrode for water oxidation. Interestingly, our synthesis provides unexpected Ni_2P nanoparticles well-anchored on $Mg_2O(OH)_2$-like phase. Several literature reports suggest that lattice strain can be realized in such systems,[10] and the resultant interfacial compression strain between the phases most likely accounts for high catalytic activity.

Our original motivation was based on the chemical similarity of Mg and transition-metal phosphides. For example, MgP_4 comprises Mg^{2+} cations sandwiched between $(P_4)^{2-}$ layers;[11] both FeP_4 and MnP_4 have similar layered crystal structures.[12] The existence of the reported ternary compound $Mg_{1.5}Ni_{12.5}P_7$, as well as the bulk compound $Mg_2Ni_{12}P_7$ that we synthesized (Figure S1 in the Supporting Information), provided additional indications that doping of Mg into Ni_2P is possible.[13] In order to understand potential changes in the electronic structure of Ni_2P, we performed density functional theory (DFT) calculations.[14] According to the calculations, Mg doping, if successful, should have a significant impact on the electronic band structure and density of states (Figure S2 in the Supporting Information).

Guided by our hypothesis, we took advantage of our earlier methodology[7,9] to prepare Mg-containing nickel phosphide catalysts supported on CP. The protocol for synthesis of the mixed/doped phosphides involves four steps: (1) hydrophilization of the intrinsically hydrophobic CP using an O_2 plasma treatment, (2) sputtering of the metals, (3) thermal annealing to alloy the metals, and (4) gas transport phosphorization. Under optimized conditions, the protocol yielded a 2.4 × 10 cm^2 piece of electrode material, denoted as as-grown (AG) sample. For comparison, we also prepared pristine Ni_2P as control. According to powder X-ray diffraction (XRD), Mg-containing Ni_2P crystallizes in the same structure type as pristine Ni_2P and not as $Mg_2Ni_{12}P_7$. In contrast, a conventional solid-state reaction of the elements in a sealed carbonized silica tube at 850 °C forms $Mg_2Ni_{12}P_7$ predominantly. Similar solid-state reactions carried out at 500 °C were unsuccessful and resulted in unreacted or partially reacted products. Powder XRD patterns recorded from the CP-supported pristine and Mg-modified Ni_2P samples are shown in Figure 1a. The refined[15] unit-cell parameters of Ni_2P were a = 5.860(5) Å, c = 3.362(4) Å, and V = 100.02(16) $Å^3$; the refined unit-cell parameters of the Mg-modified sample were a = 5.839(1) Å, c = 3.354(1) Å, and V = 99.05(5) $Å^3$. The observed modification of the unit-cell parameters may be caused by either Mg doping or by introducing strains/defects in the Ni_2P. The produced catalysts form small crystals, with sizes ranging from dozens to hundreds of nanometers over the CP fibers (Figure 1b). The energy dispersive X-ray spectrometry (EDX) maps shown in Figure 1b reveal that the elements are homogeneously distributed over the carbon fibers.

We investigated the activities of both the Mg-containing and the control Ni_2P electrodes toward the OER in an aqueous 1 M KOH solution, in order to validate the expected positive effect of Mg addition (Figure 2). We found that both electrodes exhibit high activity in water oxidation, outperforming commercial NiO, MgO, and even RuO_2 and IrO_2 samples. Notably, the Mg-modified Ni_2P catalyst shows a significantly higher activity, when compared with pure Ni_2P for a similar mass loading (Figure 2a). Specifically, the AG catalyst reaches anodic current densities of 10, 20, and 100 mA cm^{-2} at overpotentials of 0.28, 0.30, and 0.35 V, respectively, whereas the control electrode exhibits lower activity, reaching anodic current densities of 10, 20, and 100 mA cm^{-2} at higher overpotentials of 0.31, 0.33, and 0.42 V, respectively. The measured Tafel slope (T_S) values are also different (48 and 71 mV dec^{-1} for the Mg-modified and pristine Ni_2P catalysts, respectively), confirming the superior performance of the catalyst obtained upon addition of Mg (Figure 2b). We also

DOI: 10.1021/acscatal.7b01954
ACS Catal. 2017, 7, 5450−5455

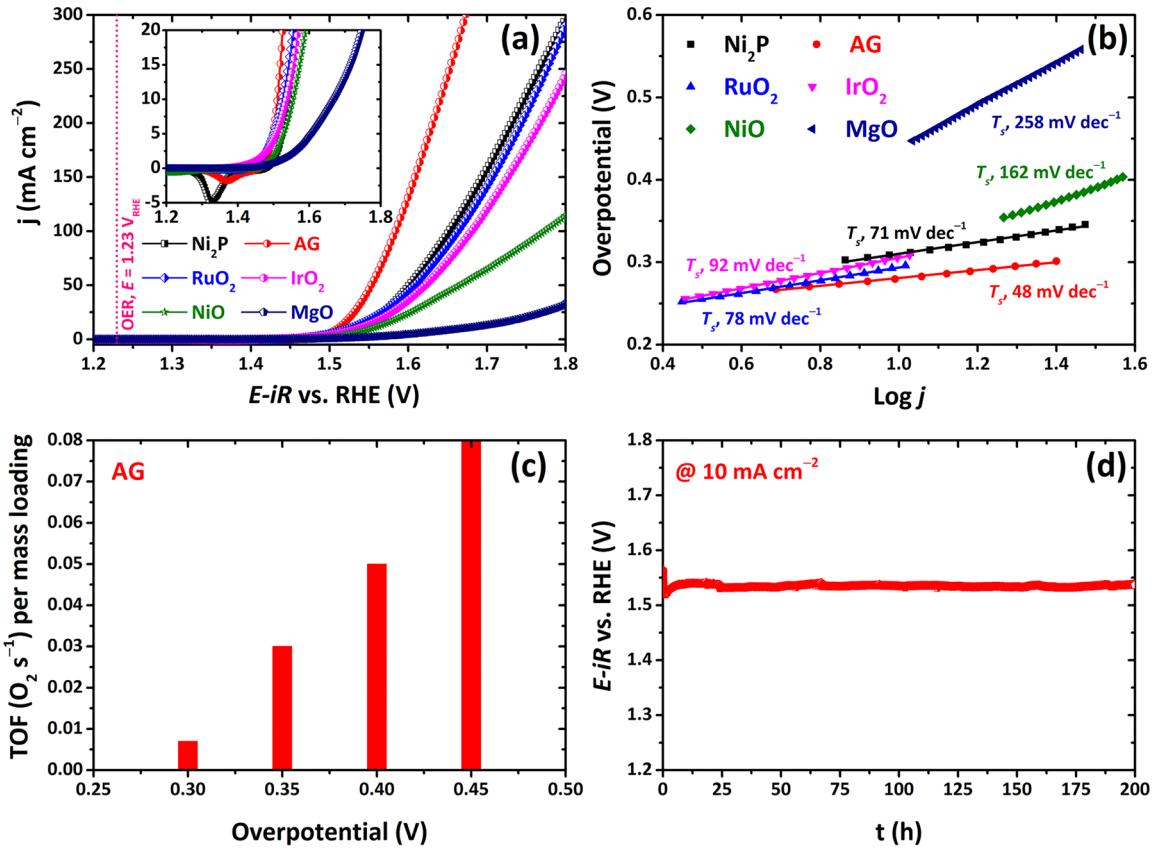

Figure 2. Water oxidation performance of CP-supported Mg-modified Ni_2P and control Ni_2P, NiO, MgO, RuO_2, and IrO_2 electrocatalysts (mass loading = 1.3 mg cm^{-1}) in an aqueous 1 M KOH electrolyte. (a) Anodic polarization curves recorded at a scan rate of 5 mV s^{-1}. The inset shows an enlargement of the potential window (1.2−1.8 V_{RHE}), which is provided for clarity. (b) Tafel plots measured for the AG and control electrocatalysts. (c) O_2 turnover frequencies per mass loading of the Mg-modified Ni_2P electrocatalyst plotted as a function of overpotential. (d) Chronopotentiometric curve indicating the high durability of the AG electrocatalyst during 200 h of galvanostatic electrolysis under a constant current density of 10 mA cm^{-2}.

estimated the O_2 turnover frequencies (TOFs) per mass loading of Mg-modified Ni_2P (Figure 2c), assuming that all of the metal ions are catalytically active. As an anode for the OER in alkaline electrolyte, the electrode shows a large turnover frequency of 0.05 s^{-1} at an overpotential of 0.4 V. Significantly, the catalyst exhibits a higher efficiency toward water oxidation at low overpotentials, increasing with anodic potential as a result of the higher current densities. Overall, the electrocatalytic data confirm the outstanding performance of the Mg-containing catalyst in water oxidation.

We then studied the stability of the AG catalyst under OER conditions. The results of galvanostatic water oxidation at 10 mA cm^{-2} for more than 8 days indicate a high electrochemical and chemical stability of the designed catalyst in harsh basic medium (high alkali resistance; see Figure 2d). An interesting effect is observed at the initial stage of durability testing: there is a 50 mV favorable drop in overpotential during the first hours of testing. This effect is likely to be associated with the immediate metal phosphide oxidation under OER conditions, leading to the generation of a stable oxide/hydroxide Mg/Ni catalyst in situ.[16]

XRD analysis of the tested Mg-modified Ni_2P catalyst revealed that the Ni_2P structure was preserved after short line scan voltammetry (LSV) testing, whereas β-NiO(OH), NiO, and $Mg_2O(OH)_2$ were observed after long durability tests (Figure 1a). The observed in situ generation of a hydroxide/oxide OER catalyst from a phosphide precursor has morphological and chemical implications. SEM studies reveal that the smaller particles disappear after the LSV testing, compared to the appearance of the AG sample (see Figure S3 in the Supporting Information). After extended galvanostatic water oxidation tests for 8 days, the catalyst contains a larger fraction of small particles, when compared to the AG catalyst (Figure S3).

In order to understand the exact microstructure and composition changes during water oxidation, scanning transmission electron microscopy (STEM) was employed to investigate the AG Mg-modified Ni_2P sample. Figure 3a shows a representative high-angle annular-dark-field (HAADF) image of the particles in the AG sample. The corresponding elemental maps reveal that the well-isolated Ni_2P nanoparticles are supported by the hexagonal (Mg,Ni)-$P_xO_y(OH)_z$ phase, which is isostructural to $Mg_2O(OH)_2$, as identified by the electron diffraction shown in Figure 3e. Thorough analysis proved that only tiny amounts of Mg, if any, are doped into the Ni_2P matrix. After the LSV testing, one prominent change observed in our experiments is that the Ni_2P particles anchored on $Mg_2O(OH)_2$-like phase immediately form a core−shell structure (Figure 3b). The corresponding elemental maps reveal that when the surface of the AG electrode is in contact with electrolyte solution upon the initial LSV testing, P is evidently leached out from both the Ni_2P nanoparticles and the (Mg,Ni)$P_xO_y(OH)_z$ support, resulting in the formation of shell layers consisting of Ni and O, which

DOI: 10.1021/acscatal.7b01954
ACS Catal. 2017, 7, 5450−5455

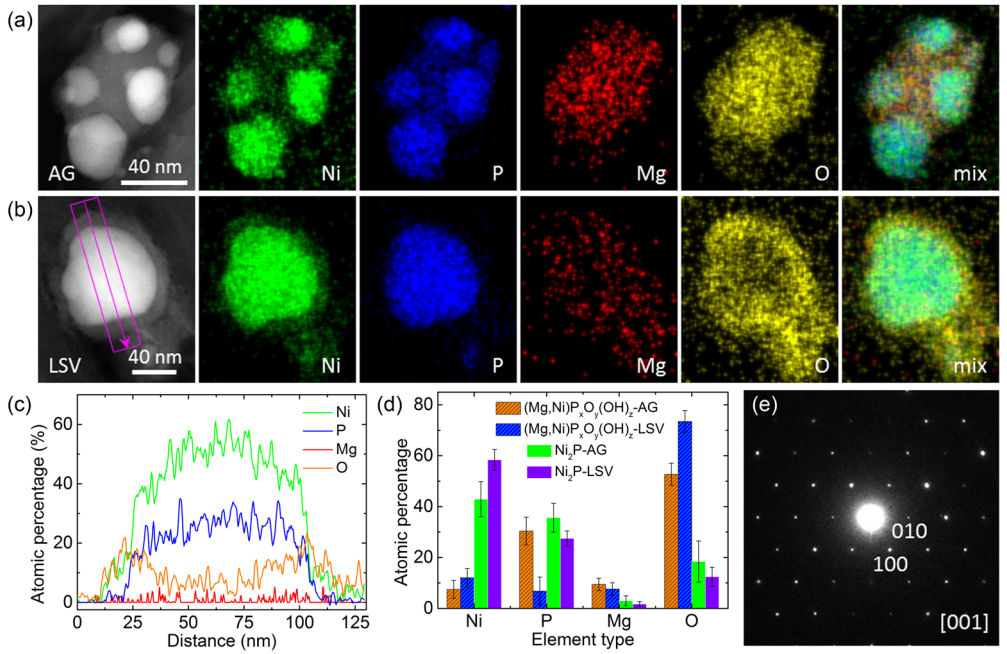

Figure 3. HAADF–STEM image of the (a) AG and (b) LSV-tested Mg-modified Ni_2P catalyst, together with the simultaneously collected EDX maps of Ni, P, Mg, O, and their mixture. (c) The elemental line profiles extracted from the LSV-tested catalyst; the position of the region of interest is indicated in panel (b). (d) Compositional analysis of the $(Mg,Ni)P_xO_y$ support and the Ni_2P particles before and after the catalytic test. (e) Electron diffraction pattern of the $(Mg,Ni)P_xO_y(OH)_z$ support, which can be completely indexed using the unit-cell parameters for hexagonal $Mg_2O(OH)_2$.

become monoclinic β-NiO(OH) and cubic NiO. The elemental line profile shown in Figure 3c clearly evidences the respective composition change and the formation of the core–shell structure. Figure 3d summarizes concentration variation of different elements before and after the LSV testing, both for the Ni_2P particles and the $(Mg,Ni)P_xO_y(OH)_z$ support.

Questions still remained concerning the active phase at the catalyst surface,[17] and to address these, we performed X-ray photoelectron spectroscopy (XPS) study of the AG Mg-modified electrode and the resultant electrode after stability testing for >8 days. The XPS data for the electrodes (Figure 4) are consistent with the interpretation of the catalyst as nanostructured Ni_2P supported on a $Mg_2O(OH)_2$-like phase. The surface of the as-prepared electrode (Figure 4a) is dominated by P compounds (elemental ratios, using Mg as a reference: Ni:Mg < 0.2, P:Mg = 6), while the Mg signal is attenuated by more than a factor of 2, suggesting that the nanostructured AG layer is covering the $Mg_2O(OH)_2$-like support. In contrast, after stability testing (Figure 4b), the surface contains an approximately constant amount of Ni and a dramatically reduced amount of P (Ni:Mg = 0.2, P:Mg = 0.1), suggesting a small number of Ni-based nanoparticles supported on MgO as the final morphology. The as-prepared electrode includes both Ni oxide and hydroxide/phosphate, as indicated by the Ni $2p_{3/2}$ components at binding energy (BE) values of ca. 853 and 857 eV, respectively,[18] while only Ni hydroxide/phosphate remains after the stability testing. The P 2p peak is broad for both electrodes, indicating at least two different P chemical states (Figure 4), one of which has a binding energy of BE = 133.8 eV, which is typical for phosphates.[18a,c,19] The second component with BE = 135.8 ± 0.2 eV corresponds to compounds with the highest oxidation state of P, such as P_2O_5.[19] The nominal Ni:P ratio after the stability testing is 2:1, suggesting that the original nanoparticles had an overall Ni_2P stoichiometry, but had been converted to a combination of Ni hydroxide/phosphate and $(Mg,Ni)P_xO_y(OH)_z$, which is consistent with electron microscopy.

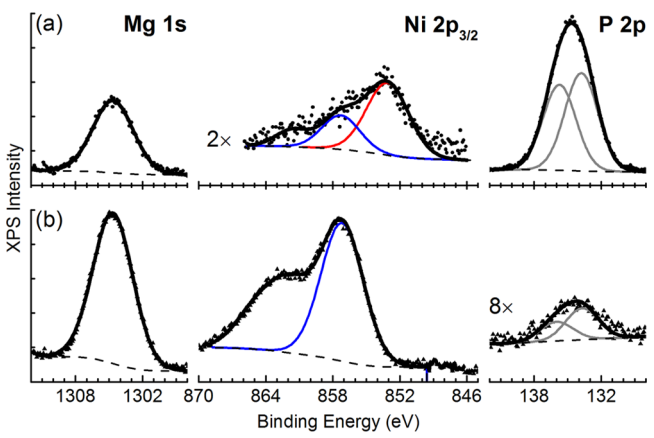

Figure 4. XPS data for synthesized Mg-modified Ni_2P electrodes: (a) as-grown and (b) after stability testing for 8 days. Spectra in Mg 1s, Ni $2p_{3/2}$, and P 2p regions are shown as raw intensities for each element, except where a multiplication factor is indicated. Symbols denote raw data, dashed lines represent background, colored lines denote highlighted fit components, and thick black lines represent the overall fit.

Based on our detailed experimental study, we hypothesized that sputtered metallic 200 nm Mg layer reacts with the moisture and oxygen from the air forming a $Mg_2O(OH)_2$-like layer underneath of the sputtered metallic 200 nm Ni layer. The subsequent alloying experiment does not result in the formation of the Mg_xNi_y alloy, because of the oxidized nature of Mg. Finally, gas transport phosphorization reaction leads to the formation of the Ni_2P nanoparticles anchored to the partially

DOI: 10.1021/acscatal.7b01954
ACS Catal. 2017, 7, 5450–5455

phosphorized mixed $Mg_2O(OH)_2$-like phase with (Mg,Ni)-$P_xO_y(OH)_z$ composition. Since the Mg almost does not incorporate into the Ni_2P structure, one can propose that the $NiO(OH)/Ni_2P@NiO/Mg_2O(OH)_2$ interface structure (Figure 3b) should be mainly responsible for the highly efficient OER over the initial as-grown electrode. Interestingly, our XRD results demonstrate that the lattice parameters of the Ni_2P nanoparticles anchored on the $Mg_2O(OH)_2$-like phase is smaller than the pristine Ni_2P phase. Seemingly, the β-$NiO(OH)/Ni_2P@NiO$ particles (Figure 3b) are suffering a compressive strain from the $Mg_2O(OH)_2$-like support, and the resultant lattice strain enhances catalytic activity.[10] The surface areas determined by BET for $NiO(OH)/Ni_2P@NiO/Mg_2O(OH)_2$ and control Ni_2P Mg-free catalysts were similar (72 and 67 $m^2\ g^{-1}$, respectively). This excludes the increase in the surface area as the reason for superior activity of Mg-containing catalyst.

In summary, we have realized a novel PGM-free catalyst with superior activity and good stability in water oxidation, when compared with state-of-the-art Earth-abundant OER catalysts (Figure 5).[20] The enhanced properties of the catalyst result from a combination of Ni_2P nanoparticles and $Mg_2O(OH)_2$-like support grown on carbon paper. During OER, the Ni_2P nanoparticles immediately oxidize through the core−shell structuring, eventually forming active and stable β-$NiO(OH)/Ni_2P@NiO$ catalyst supported on $Mg_2O(OH)_2$-like phase. We hypothesize that the high performance of the catalyst results from the development of a substantial degree of lattice strain in the core−shell nanoparticles and the realization of the supported catalyst with high surface area. Future studies will be directed toward the in situ investigation of the transformation and the mode of action of the catalyst. Most significantly, the successful utilization of the proposed Mg addition approach opens new avenues for the preparation of active, stable, and cost-effective catalysts for water oxidation.

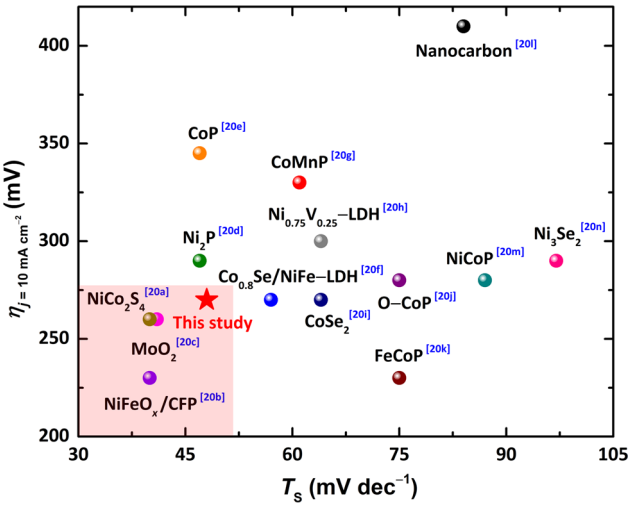

Figure 5. Comparison between the Tafel slopes and potentials required for driving current densities of 10 mA cm^{-2} for the AG catalyst with state-of-the-art OER catalysts based on Earth-abundant elements.

■ ASSOCIATED CONTENT

Supporting Information

The Supporting Information is available free of charge on the ACS Publications website at DOI: 10.1021/acscatal.7b01954.

Materials and methods, together with additional structural, theoretical, and electron microscopy data (PDF)

■ AUTHOR INFORMATION

Corresponding Author

*E-mail: yury.kolenko@inl.int.

ORCID

Xian-Kui Wei: 0000-0003-4320-1120

Kirill Kovnir: 0000-0003-1152-1912

Yury V. Kolen'ko: 0000-0001-7493-1762

Notes

The authors declare no competing financial interest.

■ ACKNOWLEDGMENTS

We thank all members of the Nanochemistry Group at the INL for their fruitful scientific and technical input. This work was supported by the European Union's Horizon 2020 research and innovation program through the CritCat Project under Grant Agreement No. 686053, as well as by ERDF COMPETE 2020 and Portuguese FCT funds under the PrintPV project PTDC/CTM-ENE/5387/2014 (Grant Agreement No. 016663). J.L.L. acknowledges financial support from SPINOGRAPH.

■ REFERENCES

(1) Cipriani, G.; Di Dio, V.; Genduso, F.; La Cascia, D.; Liga, R.; Miceli, R.; Galluzzo, G. R. *Int. J. Hydrogen Energy* **2014**, *39*, 8482−8494.

(2) (a) Sapountzi, F. M.; Gracia, J. M.; Weststrate, C. J.; Fredriksson, H. O. A.; Niemantsverdriet, J. W. *Prog. Energy Combust. Sci.* **2017**, *58*, 1−35. (b) Pomerantseva, E.; Resini, C.; Kovnir, K.; Kolen'ko, Y. V. *Adv. Phys. X* **2017**, *2*, 211−253.

(3) Reier, T.; Nong, H. N.; Teschner, D.; Schlögl, R.; Strasser, P. *Adv. Energy Mater.* **2017**, *7*, 1601275.

(4) Diaz-Morales, O.; Raaijman, S.; Kortlever, R.; Kooyman, P. J.; Wezendonk, T.; Gascon, J.; Fu, W. T.; Koper, M. T. M. *Nat. Commun.* **2016**, *7*, 12363.

(5) (a) Roger, I.; Shipman, M. A.; Symes, M. D. *Nat. Rev. Chem.* **2017**, *1*, 0003. (b) Hunter, B. M.; Gray, H. B.; Muller, A. M. *Chem. Rev.* **2016**, *116*, 14120−14136.

(6) Seh, Z. W.; Kibsgaard, J.; Dickens, C. F.; Chorkendorff, I.; Nørskov, J. K.; Jaramillo, T. F. *Science* **2017**, *355*, No. eaad4998.

(7) Costa, J. D.; Lado, J. L.; Carbó-Argibay, E.; Paz, E.; Gallo, J.; Cerqueira, M. F.; Rodríguez-Abreu, C.; Kovnir, K.; Kolen'ko, Y. V. *J. Phys. Chem. C* **2016**, *120*, 16537−16544.

(8) Xin, H. L.; Vojvodic, A.; Voss, J.; Norskov, J. K.; Abild-Pedersen, F. *Phys. Rev. B: Condens. Matter Mater. Phys.* **2014**, *89*, 115114.

(9) Lado, J. L.; Wang, X.; Paz, E.; Carbó-Argibay, E.; Guldris, N.; Rodríguez-Abreu, C.; Liu, L.; Kovnir, K.; Kolen'ko, Y. V. *ACS Catal.* **2015**, *5*, 6503−6508.

(10) (a) Stamenkovic, V. R.; Fowler, B.; Mun, B. S.; Wang, G.; Ross, P. N.; Lucas, C. A.; Marković, N. M. *Science* **2007**, *315*, 493−497. (b) Huang, X.; Zhao, Z.; Cao, L.; Chen, Y.; Zhu, E.; Lin, Z.; Li, M.; Yan, A.; Zettl, A.; Wang, Y. M.; Duan, X.; Mueller, T.; Huang, Y. *Science* **2015**, *348*, 1230−1234. (c) Li, H.; Tsai, C.; Koh, A. L.; Cai, L.; Contryman, A. W.; Fragapane, A. H.; Zhao, J.; Han, H. S.; Manoharan, H. C.; Abild-Pedersen, F.; Norskov, J. K.; Zheng, X. *Nat. Mater.* **2015**, *15*, 48−53.

(11) Gibiński, T.; Cisowska, E.; Żdanowicz, W.; Henkie, Z.; Wojakowski, A. *Krist. Tech.* **1974**, *9*, 161−163.

DOI: 10.1021/acscatal.7b01954
ACS Catal. 2017, 7, 5450−5455

(12) (a) Jeitschko, W.; Ruhl, R.; Krieger, U.; Heiden, C. *Mater. Res. Bull.* **1980**, *15*, 1755−1762. (b) Jeitschko, W.; Braun, D. J. *Acta Crystallogr., Sect. B: Struct. Crystallogr. Cryst. Chem.* **1978**, *34*, 3196−3201.
(13) Mewis, A. *Z. Naturforsch., B: J. Chem. Sci.* **1976**, *31*, 144.
(14) (a) Giannozzi, P.; Baroni, S.; Bonini, N.; Calandra, M.; Car, R.; Cavazzoni, C.; Ceresoli, D.; Chiarotti, G. L.; Cococcioni, M.; Dabo, I.; Dal Corso, A.; de Gironcoli, S.; Fabris, S.; Fratesi, G.; Gebauer, R.; Gerstmann, U.; Gougoussis, C.; Kokalj, A.; Lazzeri, M.; Martin-Samos, L.; Marzari, N.; Mauri, F.; Mazzarello, R.; Paolini, S.; Pasquarello, A.; Paulatto, L.; Sbraccia, C.; Scandolo, S.; Sclauzero, G.; Seitsonen, A. P.; Smogunov, A.; Umari, P.; Wentzcovitch, R. M. *J. Phys.: Condens. Matter* **2009**, *21*, 395502. (b) Blochl, P. E. *Phys. Rev. B: Condens. Matter Mater. Phys.* **1994**, *50*, 17953−17979. (c) Perdew, J. P.; Burke, K.; Ernzerhof, M. *Phys. Rev. Lett.* **1996**, *77*, 3865−3868. (d) http://elk.sourceforge.net.
(15) Akselrud, L.; Grin, Y. *J. Appl. Crystallogr.* **2014**, *47*, 803−805.
(16) Bernicke, M.; Eckhardt, B.; Lippitz, A.; Ortel, E.; Bernsmeier, D.; Schmack, R.; Kraehnert, R. *ChemistrySelect* **2016**, *1*, 482−489.
(17) (a) Weidler, N.; Schuch, J.; Knaus, F.; Stenner, P.; Hoch, S.; Maljusch, A.; Schafer, R.; Kaiser, B.; Jaegermann, W. *J. Phys. Chem. C* **2017**, *121*, 6455−6463. (b) Yu, X. Y.; Feng, Y.; Guan, B. Y.; Lou, X. W.; Paik, U. *Energy Environ. Sci.* **2016**, *9*, 1246−1250.
(18) (a) Pan, Y.; Liu, Y.; Zhao, J.; Yang, K.; Liang, J.; Liu, D.; Hu, W.; Liu, D.; Liu, Y.; Liu, C. *J. Mater. Chem. A* **2015**, *3*, 1656−1665. (b) Payne, B. P.; Biesinger, M. C.; McIntyre, N. S. *J. Electron Spectrosc. Relat. Phenom.* **2012**, *185*, 159−166. (c) Wang, X.; Li, W.; Xiong, D.; Petrovykh, D. Y.; Liu, L. *Adv. Funct. Mater.* **2016**, *26*, 4067−4077.
(19) He, H.; Alberti, K.; Barr, T. L.; Klinowski, J. *J. Phys. Chem.* **1993**, *97*, 13703−13707.
(20) (a) Sivanantham, A.; Ganesan, P.; Shanmugam, S. *Adv. Funct. Mater.* **2016**, *26*, 4661−4672. (b) Wang, H.; Lee, H.-W.; Deng, Y.; Lu, Z.; Hsu, P.-C.; Liu, Y.; Lin, D.; Cui, Y. *Nat. Commun.* **2015**, *6*, 7261. (c) Jin, Y. S.; Wang, H. T.; Li, J. J.; Yue, X.; Han, Y. J.; Shen, P. K.; Cui, Y. *Adv. Mater.* **2016**, *28*, 3785−3790. (d) Stern, L. A.; Feng, L. G.; Song, F.; Hu, X. L. *Energy Environ. Sci.* **2015**, *8*, 2347−2351. (e) Jiang, N.; You, B.; Sheng, M. L.; Sun, Y. J. *Angew. Chem., Int. Ed.* **2015**, *54*, 6251−6254. (f) Hou, Y.; Lohe, M. R.; Zhang, J.; Liu, S. H.; Zhuang, X. D.; Feng, X. L. *Energy Environ. Sci.* **2016**, *9*, 478−483. (g) Li, D.; Baydoun, H.; Verani, C. N.; Brock, S. L. *J. Am. Chem. Soc.* **2016**, *138*, 4006−4009. (h) Fan, K.; Chen, H.; Ji, Y.; Huang, H.; Claesson, P. M.; Daniel, Q.; Philippe, B.; Rensmo, H.; Li, F.; Luo, Y.; Sun, L. *Nat. Commun.* **2016**, *7*, 11981. (i) Liang, L.; Cheng, H.; Lei, F. C.; Han, J.; Gao, S.; Wang, C. M.; Sun, Y. F.; Qamar, S.; Wei, S. Q.; Xie, Y. *Angew. Chem., Int. Ed.* **2015**, *54*, 12004−12008. (j) Zhang, G.; Wang, G. C.; Liu, Y.; Liu, H. J.; Qu, J. H.; Li, J. H. *J. Am. Chem. Soc.* **2016**, *138*, 14686−14693. (k) Tang, C.; Zhang, R.; Lu, W.; He, L.; Jiang, X.; Asiri, A. M.; Sun, X. *Adv. Mater.* **2017**, *29*, 1602441. (l) Lai, J. P.; Li, S. P.; Wu, F. X.; Saqib, M.; Luque, R.; Xu, G. B. *Energy Environ. Sci.* **2016**, *9*, 1210−1214. (m) Liang, H. F.; Gandi, A. N.; Anjum, D. H.; Wang, X. B.; Schwingenschlogl, U.; Alshareef, H. N. *Nano Lett.* **2016**, *16*, 7718−7725. (n) Swesi, A. T.; Masud, J.; Nath, M. *Energy Environ. Sci.* **2016**, *9*, 1771−1782.

DOI: 10.1021/acscatal.7b01954
ACS Catal. 2017, 7, 5450−5455

Interface Engineering in Nanostructured Nickel Phosphide Catalyst for Efficient and Stable Water Oxidation

Junyuan Xu,[†] Xian-Kui Wei,[‡] José Diogo Costa,[†] José Luis Lado,[§] Bryan Owens-Baird,[‖] Liliana P. L. Gonçalves,[†] Soraia P. S. Fernandes,[†] Marc Heggen,[‡] Dmitri Y. Petrovykh,[†] Rafal E. Dunin-Borkowski,[‡] Kirill Kovnir,[‖] and Yury V. Kolen'ko*[,†]

[†] International Iberian Nanotechnology Laboratory, Braga 4715-330, Portugal.
[‡] Ernst Ruska-Centre for Microscopy and Spectroscopy with Electrons and Peter Grünberg Institute, Forschungszentrum Jülich GmbH, 52425 Jülich, Germany.
[§] QuantaLab, International Iberian Nanotechnology Laboratory, Braga 4715-330, Portugal.
[‖] Department of Chemistry, University of California, Davis, Davis, CA 95616, USA.
*yury.kolenko@inl.int

COMPUTATIONAL METHODOLOGY

Structure relaxation of pure Ni_2P and its 33% Mg-doped analogue was performed with density functional theory (DFT) using the Quantum Espresso simulation package[14a] with projector augmented wave pseudopotentials[14b] and the Perdew–Burke–Ernzerhof exchange correlation functional.[14c] The density of states (DOS) and electron localization function (ELF) were calculated with previously optimized structures using the all-electron linearized augmented plane wave package Elk[14d] in a *k*-mesh with $10 \times 10 \times 10$ points. The projection of the density of states (PDOS) was averaged over different atoms of the same type.

A comparison of diagrams of the elemental PDOS (Figures S2c and S2d) shows the broadening effect of Mg doping on the Ni 3d orbitals, resulting in a merging of the three original spectral peaks into one and enhancing the DOS around the Fermi energy (Figures S2g and S2h). We then analyzed the influence of chemical bonding in pure and doped Ni_2P using ELF analysis. ELF slices along (001) show that Mg substitution changes the ELF distribution around the P atoms (Figures S2e and S2f).

CHEMICALS

Carbon paper (Toray Paper 120), Mg and Ni sputtering targets (Materion), red P powder (98.9%, Alfa Aesar), MgO (nanopowder, 99+%, Alfa Aesar), NiO (nanopowder, 99.8%, Sigma-Aldrich), RuO_2 (anhydrous, 99.9%, Alfa Aesar), IrO_2 (99%, Alfa Aesar), KOH (≥85%, Sigma-Aldrich) and Pt wire (99.9%, Sigma-Aldrich) were used as received. Ultrapure water (18.2 MΩ cm^{-2}, TOC < 3 p.p.b.) was generated using a Milli-Q Advantage A10 system (Millipore). Solid state reactions were carried out using Ni powder (99.996%, Alfa Aesar), red P powder (99%, Alfa Aesar), and Mg turnings (99.98%, Alfa Aesar) as received.

SYNTHESIS AND CHARACTERIZATION OF THE CATALYSTS

Since CP is hydrophobic, it was first subjected to an O_2 plasma treatment for 5 min (Harrick Plasma), in order to increase its wetting properties in aqueous media. Next, a 200 nm layer of Mg and subsequently a 200 nm layer of Ni were sputtered onto both sides of the CP using a multitarget ultrahigh vacuum sputtering system (Kenosistec). The composite CP was then subjected to an alloying heat treatment at 600 °C for 2 h under Ar, followed by gas transport phosphorization at 500 °C for 6 h under Ar using 0.3 g of red P powder per 2.4 × 10 cm^2 of the CP specimen. The control CP-supported pristine Ni_2P catalyst was prepared in the same fashion, but without deposition of a Mg layer. The as-synthesized electrodes are denoted as-grown (AG) and Ni_2P for convenience. The resulting mass densities of the Mg-modified Ni_2P and control pure Ni_2P catalysts were gravimetrically (Cubis MCM36, Sartorius) estimated to be 1.33 mg cm^{-2} and 1.16 mg cm^{-2}, respectively. The specific surface area of the CP-supported Mg-modified Ni_2P and control pure Ni_2P were measured to be about 72 $m^2 g^{-1}$ and 67 $m^2 g^{-1}$, respectively (Autosorb iQ_2, Quantachrome).

The catalysts were analyzed using powder X-ray diffraction (XRD, X'Pert PRO, PANalytical), scanning electron microscopy (SEM, JSM-7400F, JEOL) and high-angle annular dark-field scanning transmission electron microscopy (HAADF–STEM, Titan 80-200 Chemi-STEM, FEI) equipped with a Super-X energy dispersive X-ray spectrometer (EDX), as well as inductively coupled plasma – optical emission spectroscopy (ICP–OES, ICPE-9000, Shimadzu). According to the ICP–OES results, the molar ratio between Mg and Ni was estimated to be 0.24 in Mg-modified Ni_2P catalyst. Unit cell refinements were performed with WinCSD[15] using a Ge internal standard. The X-ray photoelectron spectroscopy (XPS) measurements were performed using a monochromated microfocused Al *K*α X-ray source that defined an analysis spot of ca. 900 × 600 μm^2. All spectra were acquired in normal emission with an effective analyzer collection angle of ≈ 30°. Aliphatic C 1s peak was observed at binding energy (BE) of 284.5 ± 0.3 eV without the use of charge neutralization, indicating the absence of overall sample charging. The peaks were broadened, however, for all the elements by about 2× compared to the values for similar systems, suggesting heterogeneity of electrical conductivity across the sample.

Solid state synthesis of Mg-doped Ni_2P was carried out through direct reaction of the elements. Two samples were prepared with a Ni:Mg:P ratio of 1.6:0.4:1 and loaded into carbonized silica ampoules in air, evacuated and flame-sealed. The first ampoule was heated to 850 °C over 10 h, annealed at this temperature for 96 h, cooled to 600 °C over 24 h, and cooled to room temperature in the turned-off furnace. The second ampoule was heated to 500 °C over 10 h, annealed at this temperature for 96 h, and cooled to room temperature in the turned-off furnace. The samples were

analyzed by XRD using a Rigaku Miniflex 600 diffractometer employing
Cu-*K*α radiation.

ELECTROCHEMICAL EXPERIMENTS

Electrochemical water oxidation experiments were carried out at room temperature in a three electrode assembly using a geometrically well-defined piece of C paper with the supported catalyst as the working electrode, a Pt wire as the counter electrode and a saturated calomel electrode (SCE) as the reference electrode. The electrolyte was aq. 1 M KOH. For comparison, the electrocatalytic performance of commercial high surface area RuO_2, IrO_2, NiO and MgO materials supported on a carbon paper (loading: 1.3 mg cm^{-2}) was also evaluated. The measurements were controlled with a potentiostat/galvanostat (VMP-3, Biologic) while carrying out linear sweep voltammetry (LSV) at 5 mV s^{-1} in the range 1.2 to 1.8 V_{RHE}, applying 85% internal-resistance (*iR*) compensation. The *iR* values were measured by single-point high-frequency impedance measurements. The durability test was performed using galvanostatic electrolysis at a fixed current density of 10 mA cm^{-2} while monitoring the variation of overpotential for 200 h.

O_2 TOFs per mass loading of Mg-modified Ni_2P catalyst were estimated according to the equation TOF (O_2 s^{-1}) = (jA)/(4Fn), where j is the current density at a given overpotential (A cm^{-2}), A is the surface area of the electrode (1.0 cm^2), F is the Faraday constant (96500 C mol^{-1}), and n is the mole number of the metal in the electrode (mol). The n was determined from the equation n = 1.33 10^{-3} g cm^{-2} * 1.0 cm^2 / metal molar mass. We assumed that all of the metal ions were catalytically active, although in reality most likely that some metal sites are inaccessible for water oxidation, and thus the calculated TOF represents the lowest estimated value.

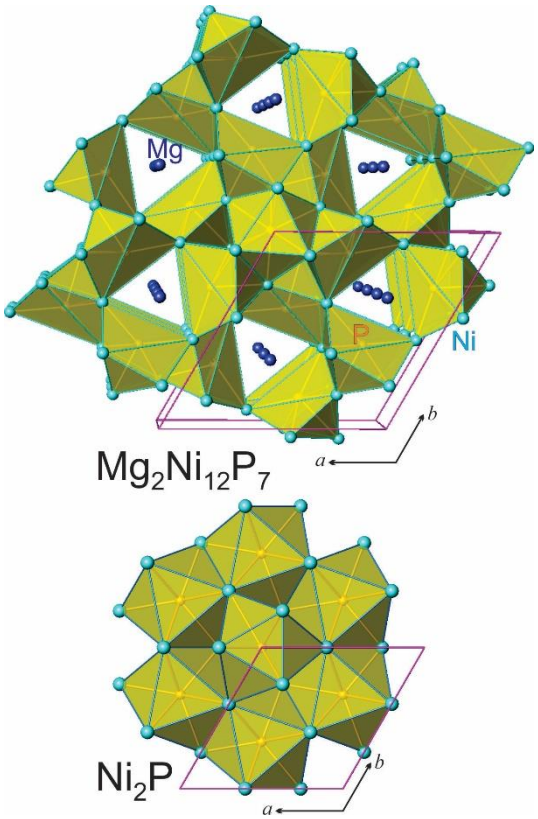

Figure S1. Polyhedral representations of the crystal structures of $Mg_2Ni_{12}P_7$ and Ni_2P viewed along the [001] direction. Unit cells are shown with purple lines. Mg: blue; Ni: cyan; P: yellow. In the crystal structure of $Mg_2Ni_{12}P_7$ (~$[Mg_{0.14}Ni_{0.86}]_2P$), one third of the P atoms are coordinated by 9 Ni atoms, which is similar to the coordination of P atoms in Ni_2P. The other two thirds of the P atoms are coordinated in a similar manner, but by 7 Ni + 2 Mg atoms.

FIGURES

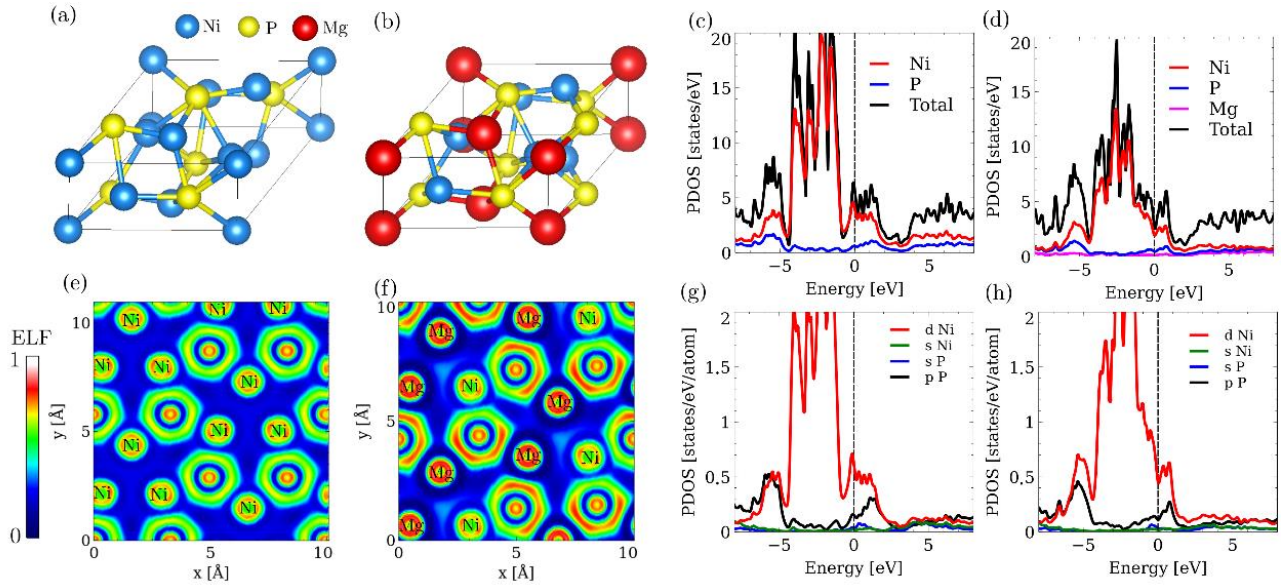

Figure S2. Atomic structure, PDOS diagrams, and ELF slices along the (001) plane of pure Ni_2P (a, e, c) and its relaxed 33% Mg-doped $Ni_4Mg_2P_3$ analog (b, f, d). Comparisons of the partial contributions of Ni 3*d*, Ni 4*s*, P 3*s*, and P 3*p* are shown in (g) for pure Ni_2P and in (h) for 33% Mg-doped Ni_2P.

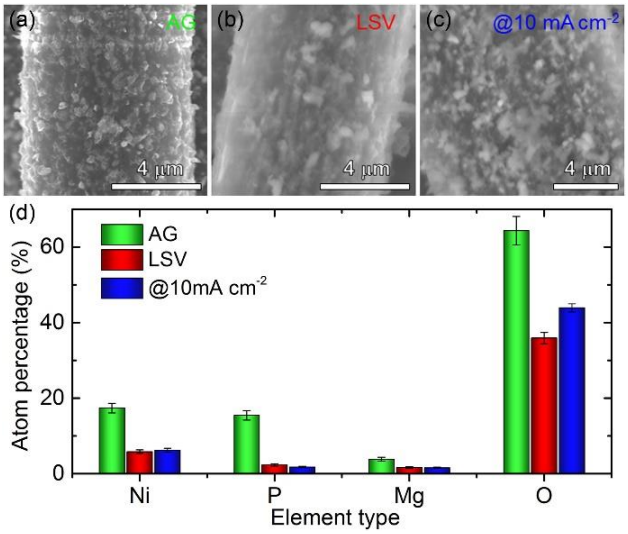

Figure S3. High magnification SEM images of (a) the as-grown (AG), (b) the LSV- and (c) the durability-tested (@10 mA cm^{-2}) Mg-modified Ni_2P catalyst. (d) Comparison of the mass percentage of elements before and after the electrochemical tests.